Experimental Glaucoma Causes Optic Nerve Head Neural Rim Tissue Compression: A Potentially Important Mechanism of Axon Injury

Brad Fortune,[1] Juan Reynaud,[1] Christy Hardin,[1] Lin Wang,[1] Ian A. Sigal,[2] and Claude F. Burgoyne[1]

[1]Discoveries in Sight Research Laboratories, Devers Eye Institute and Legacy Research Institute, Legacy Health, Portland, Oregon, United States
[2]Department of Ophthalmology, University of Pittsburgh, Pittsburgh, Pennsylvania, United States

Correspondence: Brad Fortune, Discoveries in Sight Research Laboratories, Devers Eye Institute and Legacy Research Institute, 1225 NE Second Avenue, Portland, OR 97232, USA; bfortune@deverseye.org.

Submitted: May 25, 2016
Accepted: July 19, 2016

Citation: Fortune B, Reynaud J, Hardin C, Wang L, Sigal IA, Burgoyne CF. Experimental glaucoma causes optic nerve head neural rim tissue compression: a potentially important mechanism of axon injury. *Invest Ophthalmol Vis Sci*. 2016;57:4403–4411. DOI:10.1167/iovs.16-20000

Purpose. We tested the hypothesis that experimental glaucoma (EG) results in greater thinning of the optic nerve head (ONH) neural rim tissue than the peripapillary retinal nerve fiber layer (RNFL) tissue.

Methods. Longitudinal spectral-domain optical coherence tomography (SDOCT) imaging of the ONH and peripapillary RNFL was performed every other week under manometric IOP control (10 mm Hg) in 51 nonhuman primates (NHP) during baseline and after induction of unilateral EG. The ONH parameter minimum rim area (MRA) was derived from 80 radial B-scans centered on the ONH; RNFL cross-sectional area (RNFLA) from a peripapillary circular B-scan with 12° diameter.

Results. In control eyes, MRA was 1.00 ± 0.19 mm^2 at baseline and 1.00 ± 0.19 mm^2 at the final session ($P = 0.77$), while RNFLA was 0.95 ± 0.09 and 0.95 ± 0.10 mm^2, respectively ($P = 0.96$). In EG eyes, MRA decreased from 1.00 ± 0.19 mm^2 at baseline to 0.63 ± 0.21 mm^2 at the final session ($P < 0.0001$), while RNFLA decreased from 0.95 ± 0.09 to 0.74 ± 0.19 mm^2, respectively ($P < 0.0001$). Thus, MRA decreased by 36.4 ± 20.6% in EG eyes, significantly more than the decrease in RNFLA (21.7 ± 19.4%, $P < 0.0001$). Other significant changes in EG eyes included increased Bruch's membrane opening (BMO) nonplanarity ($P < 0.05$), decreased BMO aspect ratio ($P < 0.0001$), and decreased MRA angle ($P < 0.001$). Bruch's membrane opening area did not change from baseline in either control or EG eyes ($P = 0.27$, $P = 0.15$, respectively).

Conclusions. Optic nerve head neural rim tissue thinning exceeded peripapillary RNFL thinning in NHP EG. These results support the hypothesis that axon bundles are compressed transversely within the ONH rim along with glaucomatous deformation of connective tissues.

Keywords: glaucoma, optical coherence tomography, retinal ganglion cell axons, optic nerve head, retinal nerve fiber layer

Optical coherence tomography (OCT) can provide cross-sectional images through living tissues, such as the retina and optic nerve head (ONH), and, thus, a means of performing three-dimensional morphometry of clinically important anatomic structures. This has proven beneficial for glaucoma research and clinical care by enabling quantitative measurements of ONH and retinal nerve fiber layer (RNFL) tissues to be obtained rapidly and reliably.[1–6]

One approach to quantifying ONH neuroretinal rim tissue thickness from OCT scans is based on minimum distance mapping, as first proposed by Povazay et al.[7] Chen[8] applied this concept and reported that the thickness of the ONH rim "minimum distance band" was well correlated with the cup-disc ratio determined from color photographs and with the severity of visual field damage in glaucoma. Other studies have shown that minimum distance–based measurements of ONH rim thickness offer enhanced diagnostic power for glaucoma[9] as well as stronger correlations with visual field sensitivity[10,11] and peripapillary RNFL thickness[10] compared to other ONH neuroretinal rim parameters.

A fundamental strength of the minimum distance–based measurement is its geometric foundation,[5,7,8,12] which dictates that it should represent a perpendicular slice through the trajectory of the axon bundles as they traverse the ONH rim toward entry to the scleral canal. Peripapillary RNFL thickness measured along the A-lines of a 3.45-mm diameter circular OCT scan path centered on the ONH also should be nearly perpendicular (6° from perpendicular) to the same axon bundles (albeit containing ~1.5% fewer axons, since those arising from ganglion cells located inside the circular scan path would not be included). Hence, both measurements should be correlated strongly with the number of ganglion cell axons[12] and have approximately the same total cross-sectional area, assuming that the proportion of other nonaxonal tissue constituents, such as glial content, capillaries, and larger blood vessels, also is similar at each site.[13–15] This concept is an extension of the demonstration by Patel et al.[16] that the total cross-sectional area of RNFL tissue measured by OCT essentially is constant (independent of eccentricity) for at least 600 μm from the rim margin.

This work is licensed under a Creative Commons Attribution-NonCommercial-NoDerivatives 4.0 International License.

Because the total cross-sectional area of peripapillary RNFL tissue and ONH rim tissue should have similar content and magnitude, and can be quantified by OCT using a similar approach, we took the opportunity in this study to use OCT to test the hypothesis that glaucomatous deformation of ONH and peripapillary connective tissues results in greater thinning of the ONH neural rim tissue than the peripapillary RNFL tissue. If axon loss alone was the only factor contributing to structural change at these two adjacent sites, they should manifest equivalent loss of total cross-sectional area. The corollary to this hypothesis is that glaucomatous ONH deformation causes axon bundles to be compressed and/or stretched within the prelaminar neural rim.

Methods

Subjects

The primary cohort of animals whose data are the basis for this study has been described in detail recently.[12] It consists of 51 rhesus macaque monkeys (*Macaca mulatta*), 40 female and 11 male, ranging in age from 1.2 to 22.6 years (median, 9.6 years). Data from a secondary group of $N = 4$ adult rhesus macaques with unilateral orbital optic nerve transection[17–19] also were included for analytical comparison to experimental glaucoma (EG). All procedures were performed in strict accordance with the recommendations in the Guide for the Care and Use of Laboratory Animals of the National Institutes of Health (NIH; Bethesda, MD, USA) and were approved and monitored by the Institutional Animal Care and Use Committee (IACUC) at Legacy Health (USDA license 92-R-0002 and OLAW assurance A3234-01). All experimental methods and animal care procedures also adhered to the Association for Research in Vision and Ophthalmology's (ARVO) Statement for the Use of Animals in Ophthalmic and Vision Research.

Experimental Design and Protocol

Each animal had a minimum of three weekly baseline spectral-domain optical coherence tomography (SDOCT) imaging sessions, which are described below. Argon laser photocoagulation then was applied to the trabecular meshwork of one eye of each animal to induce chronic elevation of IOP.[20,21] Initially, 180° of the trabecular meshwork was treated in one session, then the remaining 180° was treated in a second session approximately 2 weeks later. If necessary, laser treatments were repeated in subsequent weeks (limited to a 90° sector) until an IOP elevation was first noted or if the initial postlaser IOP had returned to normal levels. The average number of laser treatments (± SD) was 5.6 ± 2.7. After initiation of laser photocoagulation, SDOCT imaging was repeated approximately every 2 weeks until euthanasia. The stage of EG at euthanasia was predetermined for each animal based on the primary study to which it was assigned. Because there were four such primary studies with differing targets for postmortem histopathology, the combined cohort provided a relatively wide range of damage for the cross-sectional analysis of this study.[12]

Anesthesia

All experimental procedures began with induction of general anesthesia using ketamine (10–25 mg/kg intramuscularly [IM]) in combination with either xylazine (0.8–1.5 mg/kg IM) or midazolam (0.2 mg/kg IM), along with a single injection of atropine sulfate (0.05 mg/kg IM). Animals then were intubated with an endotracheal tube to breathe a mixture of 100% oxygen, air and 1% to 2% isoflurane gas to maintain anesthesia to effect and oxyhemoglobin saturation as close to 100% as possible. Intravenous fluids (lactated Ringer's solution, 10–20 mL/kg/h) were administered via the saphenous vein. Vital signs were monitored throughout and recorded every 10 to 15 minutes, including heart rate, blood pressure, arterial oxyhemoglobin saturation, end tidal CO_2, and body temperature. Body temperature was maintained at 37°C, heart rate above 75 beats per minute, and oxygen saturation above 95%.

IOP Measurements

Intraocular pressure was measured in both eyes at the start of every session using a Tonopen XL (Reichert Technologies, Inc., Depew, NY, USA). The value recorded for each eye was the average of three successive measurements.

SDOCT Imaging

All SDOCT scans were acquired using a Spectralis instrument (Heidelberg Engineering, GmbH, Heidelberg, Germany) 30 minutes after IOP was manometrically stabilized to 10 mm Hg. This is important to minimize elastic components of deformation that are known to exert a greater effect on the ONH than on peripapillary RNFL thickness.[22,23] A clear, rigid gas permeable contact lens filled with 0.5% carboxymethylcellulose solution was placed over the apex of each cornea. Spectral-domain OCT scans recorded at each session included an 80-radial B-scan pattern centered on the ONH (30° wide, 1536 A-scans/B-scan, Figs. 1A, 1B) and a peripapillary circular B-scan with 12° diameter (1536 A-scans, Fig. 1E). In all cases, nine to 16 individual sweeps were averaged in real time to form each B-scan. At the first baseline imaging session, SDOCT scans were centered manually on the ONH by the operator. All follow-up scans were acquired at the same location as baseline using the instrument's automatic active eye tracking software.

Image segmentation was performed manually offline using custom software (ATL 3D Suite). For ONH radial scans, two image features in particular required segmentation for the quantitative measurements used in this study: the inner limiting membrane (ILM; yellow lines in Figs. 1A–AC) and the pair of Bruch's membrane opening points (BMO; red dots in Figs. 1A–AC) of each B-scan. Figures 1A and 1B, respectively, show a horizontally oriented B-scan and a vertically oriented B-scan through the ONH at the first baseline session (left column) and at the final time point (right column) for a single representative EG eye (i.e., whose data are close to the average effect among the entire group of $N = 51$). Each of the green line segments in Figures 1A to 1C represents the minimum rim width (MRW) vector defined as the shortest distance from the BMO point to the ILM segmentation within the plane of the B-scan. The ONH parameter minimum rim area (MRA; Fig. 1D) was derived in a similar manner as MRW; that is, two measurements for each radial B-scan, as described previously in detail.[10,24,25] In brief, the MRA for each ONH at each imaging session was represented by the sum of the areas of 160 contiguous individual trapezoids whereby the base of each trapezoid is centered on the corresponding BMO point, and the height of each trapezoid is defined as the distance between the BMO point and the ILM segmentation that minimizes the area of the trapezoid (Fig. 1D).[10]

Two image features of each peripapillary circular B-scan required segmentation for this study: the ILM and the posterior boundary of the RNFL (Fig. 1E), as described previously.[26–28] The total cross-sectional area of the peripapillary RNFL (RNFLA, Fig. 1F) was derived from the circular B-scan by measuring the distance between the ILM and posterior RNFL and multiplying the average thickness (of 1536 A-line samples) by the scan circumference (9.37 mm, which assumes a visual

Investigative Ophthalmology & Visual Science

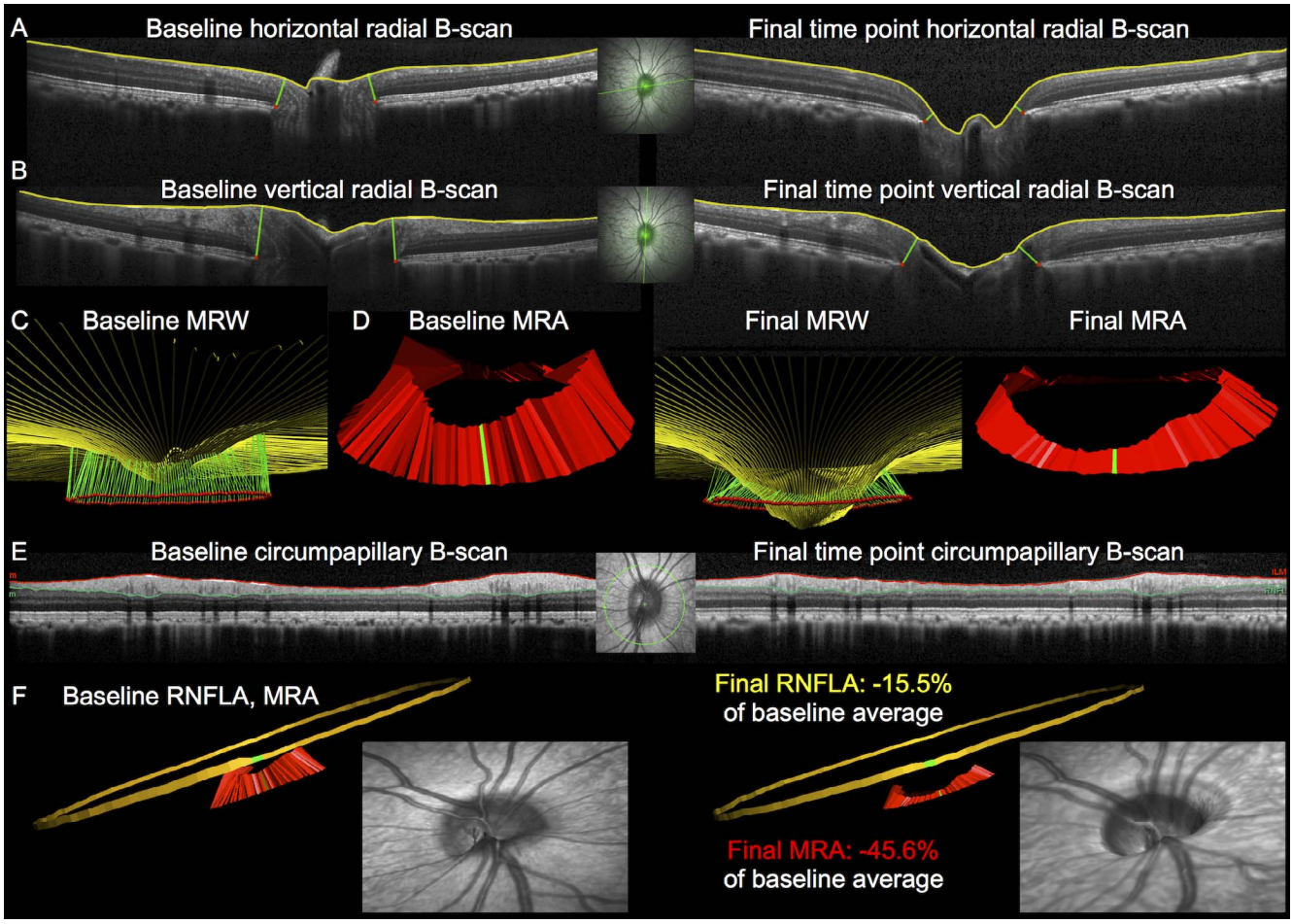

Figure 1. Methods used to quantitatively compare MRA to RNFLA. The *left column* shows baseline data, the *right column* shows final follow-up data. (**A**) B-scan through the horizontal meridian of the ONH. The *inset* shows the B-scan location indicated by the *bold green line* overlaid onto the infrared confocal scanning laser ophthalmoscopy (CSLO) reflectance image. Structures delineated in each radial B-scan include the ILM (*yellow*) and BMO points (*red*). The *green segments* connecting BMO points to the ILM represent the pair of MRW measurements made in each radial B-scan. (**B**) B-scan through the vertical meridian of the ONH. (**C**) Results for all 80 B-scans shown projected from 3D. (**D**) Derivation of MRA from the 160 radial trapezoidal sectors of each ONH (see Methods text for details). Note deformation of the ONH apparent in the right column for MRW/MRA, including a deeper "cup" and thinner "rim." In this EG eye, global average MRA decreased from 1.16 mm^2 at baseline to 0.63 mm^2 at the final time point (–45.6%). (**E**) Segmentation of peripapillary circular B-scans to obtain the parameter RNFLA are shown for the same eye and time points, ILM (*red*), and posterior RNFL boundary (*green*). Retinal nerve fiber layer thickness decreased from 113.8 μm at baseline to 96.1 μm at the final time point; RNFLA decreased from 1.07 mm^2 at baseline to 0.90 mm^2 at the final time point (–15.5%). (**F**) Retinal nerve fiber layer area represented by the *gold colored ribbon* in projected 3D image from baseline (*left*) and final time point (*right*). The much larger decrease in MRA than RNFLA suggests substantial transverse compression of axons (and possibly also astrocytes) at the ONH rim. This can be appreciated by comparison of the images inset at the bottom of each column, which are the infrared CSLO reflectance image painted onto the ILM surface at each time point; the RNFL appears stretched over the ONH rim at the final time point.

angle for the macaque eye of 247.7 μm/deg, the same transverse scaling applied for MRA measurements).

In total, there were 605 ONH SDOCT volumes analyzed in this study with a median scan quality score of 29.8 dB and interquartile range of 27.6 to 32.0 dB; the lowest scan quality score was 17.6 dB, which was the only value below 20 dB. The peripapillary circle scans had a median scan quality score of 31.3 dB and interquartile range of 27.9 to 34.3 dB; fewer than 1% had a score below 20 dB, the lowest of which was 13.9 dB.

Analysis and Statistics

Statistical analysis was performed using a commercial software package (Prism 5; GraphPad Software, Inc., La Jolla, CA, USA). For each instance of reported results, the specific statistical test applied and the corresponding *P* value are included. The fundamental null hypothesis forming the basis for this study states that the cross-sectional area of peripapillary RNFL tissue will change by exactly the same amount as the cross-sectional area of ONH rim tissue if the only structural change contributing to each is loss of retinal ganglion cell axons (since fewer than ~1.5% of retinal ganglion cells are located proximal to the location of the peripapillary RNFL scan).

Results

Figure 1 provides an individual example of results for a representative EG eye selected because its results are close to the average observed across the whole group. For each Figure (Fig. 1A–F), the left side shows results from the first baseline session and the right side shows results from the final session. Figure 1A shows one of the 80 radial B-scans through the ONH (a section close to the horizontal) and Figure 1B shows another section close to the vertical. The pair of green line

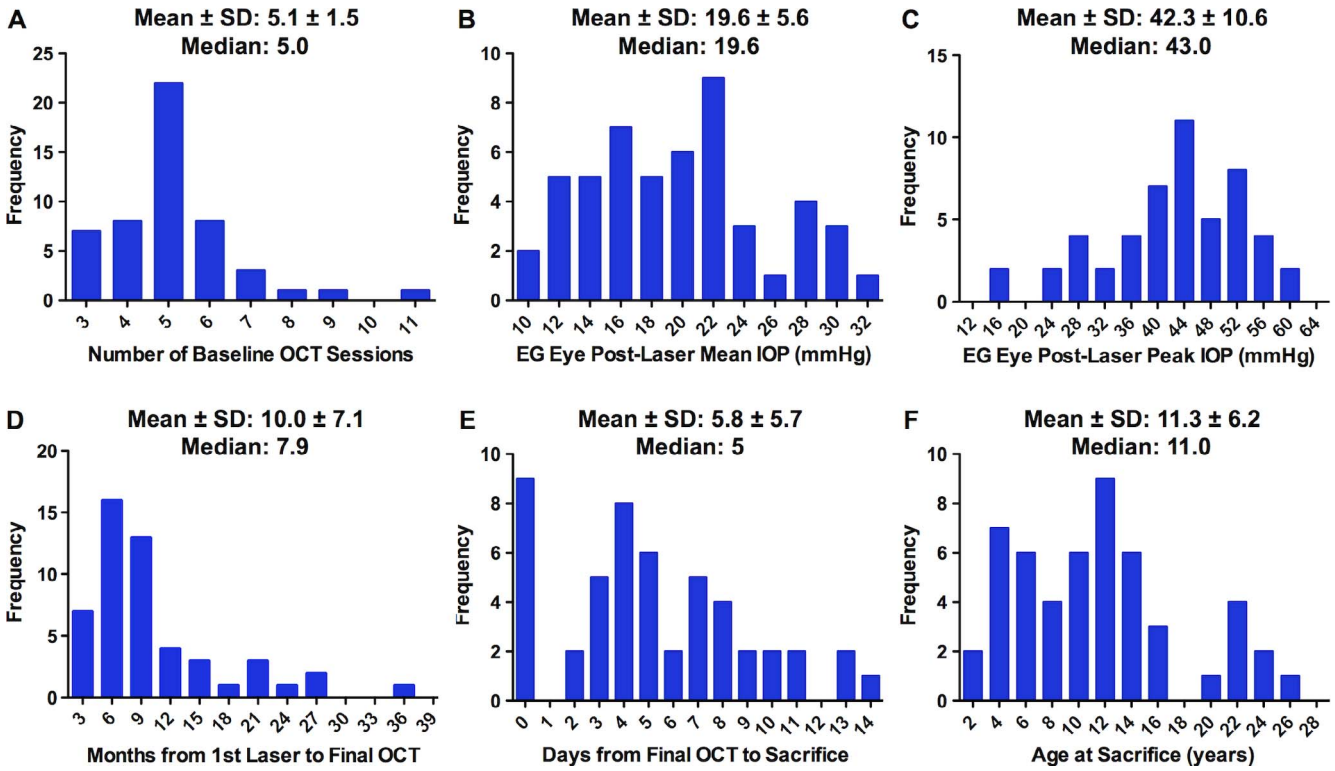

FIGURE 2. Experimental parameters for entire group ($N = 51$ NHP). Frequency histograms show (**A**) the number of baseline OCT imaging sessions per animal, (**B**) the postlaser mean IOP in EG eyes, (**C**) the postlaser peak IOP in EG eyes, (**D**) duration of follow-up (number of months between first laser and final OCT imaging session), (**E**) number of days between final OCT imaging session and euthanasia, (**F**) age at the end of the experiment.

segments in each B-scan represent the MRW measurements. These B-scans clearly show posterior deformation of the ONH surface at the final time point. Figure 1C shows a projection of the complete 3D set based on the segmentations of all 80 B-scans. At the final time point, several aspects of glaucomatous "cupping" are apparent in Figure 1C, including substantial posterior deformation of the ONH surface (shown by the change in the yellow ILM segmentation lines), thinning of the ONH rim tissue as represented by the shortened MRW vectors, axial "bowing" of the BMO into a more saddle-shaped opening and a decrease in the MRW angle, which had become more acute (i.e., the green lines are oriented more toward the plane of the BMO). Figure 1D shows the MRA results, which also show signs of glaucomatous "cupping," such as a reduced rim area with a corresponding increase in "cup" area, as well as reduced MRA angle (the red-colored trapezoids representing the 160 MRA measurements are oriented more toward the BMO plane at the final time point). Figure 1E shows the peripapillary circular B-scan at the baseline and final time points unwrapped and splayed out in typical fashion, along with the segmentations of RNFL tissue used to measure the total RNFLA. Figure 1F shows a projected 3D image with this ribbon of RNFL tissue area represented as a gold band surrounding the ONH MRA. In this EG eye, RNFLA had decreased from 1.07 mm^2 at baseline to 0.90 mm^2 at the final time point (–15.5%). Minimum rim area had decreased from 1.16 mm^2 at baseline to 0.63 mm^2 at the final time point (–45.6%). The degree of glaucomatous ONH deformation in this EG eye also can be appreciated in the more familiar clinical view presented as insets adjacent to the 3D projections in Figure 1F.

Figure 2 graphically depicts important experimental parameters for the entire group of 51 nonhuman primates (NHPs). The number of baseline OCT imaging sessions per animal ranged from 3 to 11 (median, 5; Fig. 2A). Mean IOP over the span of postlaser follow-up ranged from 10.4 to 31.0 mm Hg in EG eyes (median, 19.6 mm Hg; Fig. 2B). Mean IOP over the same period in the fellow control eyes ranged from 8.4 to 23.3 mm Hg (median, 11.4 mm Hg). The peak IOP observed during the postlaser follow-up period ranged from 15.3 to 60.3 mm Hg in EG eyes (median, 43.0 mm Hg; Fig. 2C) and from 10.0 to 31.3 mm Hg in fellow control eyes (median, 15.3 mm Hg). The duration of postlaser follow-up ranged from 3 to 37 months (median, 7.9 months; Fig. 2D). Total study duration ranged from 7 to 46 months (median, 13 months). The median time between the final imaging session and euthanasia was 5 days (range, 0 to 14 days; Fig. 2E). Age at the end of the experiment ranged from 2 to 26 years (median, 11.0 years; Fig. 2F).

Figure 3 shows the distribution of raw parameter values found at baseline (hatched boxes) and at the final imaging session for the entire group of $N = 51$ NHPs. As predicted by the hypothesis, the total cross-sectional area of ONH rim tissue was very close to the total cross-sectional area of peripapillary RNFL tissue (~1.0 mm^2), though the population variance was larger for MRA than for RNFLA. Figure 3 also shows that MRA and RNFLA parameter values are repeatable from baseline to the final session in control eyes. In control eyes, MRA was 1.00 ± 0.19 mm^2 at baseline and 1.00 ± 0.19 mm^2 at the final session ($P = 0.77$, paired t-test). Minimum rim area decreased in EG eyes from 1.00 ± 0.19 mm^2 at baseline to 0.63 ± 0.21 mm^2 at the final session ($P < 0.0001$). Retinal nerve fiber layer area in control eyes was 0.95 ± 0.09 mm^2 at baseline and 0.95 ± 0.10 mm^2 at the final session ($P = 0.96$). Retinal nerve fiber layer area decreased in EG eyes from 0.95 ± 0.09 mm^2 at baseline to 0.74 ± 0.19 mm^2 at the final session ($P < 0.0001$).

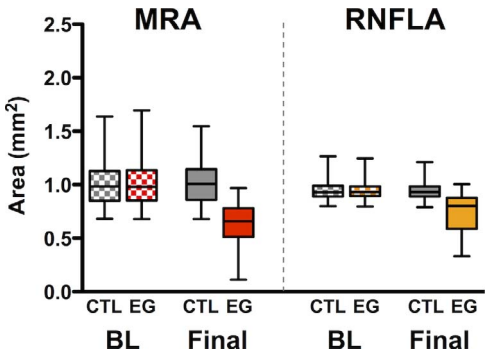

FIGURE 3. Longitudinal change in minimum rim area (MRA, *left*) versus RNFL area (RNFLA, *right*). Box plots represent the distribution (median, interquartile range, and extremes, $N = 51$) of raw parameter values in control eyes (CTL) and eyes with EG at baseline (BL, *hatched*) and at the final imaging session (MRA for EG eyes in *solid red*, RNFLA for EG eyes in *solid gold* to match Fig. 1 color scheme).

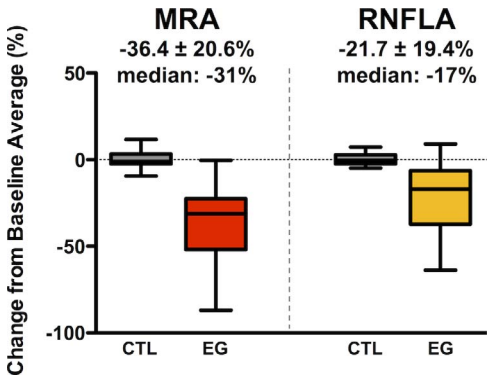

FIGURE 4. Longitudinal change in MRA (*left*) versus RNFLA (*right*) expressed relative to baseline values. Box plots represent the distribution (median, interquartile range and extremes, $N = 51$) of changes in parameter values at the final imaging session expressed as a percentage of the baseline average value for each eye. Control eyes (CTL) shown in *gray* and eyes with EG are shown in *red* for MRA and in *gold* for RNFLA. The group average (± SD) and median values of change are listed for the EG eyes.

In Figure 4 the magnitude of longitudinal MRA change is compared to the magnitude of RNFLA change. Minimum rim area decreased by 36.4 ± 20.6% in EG eyes, which was significantly more than the RNFLA decrease (21.7 ± 19.4%, $P < 0.0001$, paired *t*-test). Although these distributions of change passed a formal normality test in both cases ($P = 0.36$ for MRA, $P = 0.06$ for RNFLA, D'Agostino and Pearson omnibus test), the latter was borderline for RNFLA, so the data also were compared nonparametrically, which also found that the MRA change (median decrease of 31%) was significantly greater than the RNFLA change (median decrease of 17%, $P < 0.0001$, Wilcoxon matched-pairs signed rank test). Notwithstanding that there was a significant difference between the magnitude of MRA loss versus RNFLA loss, longitudinal change for these two parameters was strongly correlated (Pearson $R = 0.84$; 95% confidence interval, 0.74–0.91; $P < 0.0001$).

In Figure 5A the magnitude of longitudinal RNFLA change at the final session is plotted against the magnitude of MRA change for EG eyes (in red) and fellow control eyes (in blue). The vertical dashed gray line represents the lower limit of the 95% range of test–retest repeatability for MRA at baseline (±12%)[12] while the horizontal dashed gray line represents the same for RNFLA (±7.0%).[12,26,28] None of the control eyes exhibit longitudinal change at the final session beyond the limit for either parameter, thus the specificity of MRA and RNFLA is 100%. Among the group of $N = 51$ EG eyes, 45 (88%) had significantly decreased MRA while only 38 (75%) had significantly decreased RNFLA ($P = 0.04$, *z*-test to compare proportions). The dashed black diagonal line represents the 1:1 locus where all points would plot if the MRA change equaled the RNFLA change in each eye. The control eye data scatter around that line near the 0,0 point. The EG eyes, however, are shifted to the left of the 1:1 line indicating a greater degree of MRA loss compared to RNFLA loss throughout the wide range of damage studied in this group. The solid red line represents the result of Deming regression applied to the EG eye data; the slope is 1.01 (not significantly different from 1.0) and the *x*-intercept (where $y = 0$) is –15%, indicating that MRA change is approximately 15% worse than RNFLA change across nearly the entire dynamic range of these parameters. The differential between MRA change and RNFLA change was unrelated to age ($R^2 < 0.01$, $P = 0.72$), sex ($R^2 = 0.01$, $P = 0.41$), mean IOP ($R^2 = 0.06$, $P = 0.08$), or peak IOP ($R^2 = 0.02$, $P = 0.31$) when these variables were each considered alone or in combination in multiple linear regression models. Collectively, the data analysis presented in Figures 3 to 5 robustly support rejection of the null hypothesis of this study.

We performed the same analysis on data from four NHP obtained 50.3 ± 1.0 days after unilateral optic nerve transection (ONT; see recent reports for detailed description of cohort and ONT procedures).[17–19] Figure 5B shows that all four of the ONT eyes plot to the right of the 1:1 line indicating that they exhibit greater loss of peripapillary RNFLA (–42.4% ± 2.4%) than they do loss of ONH MRA (–24.3% ± 4.2%, $P = 0.0005$).

Finally, as described in Figure 1 for the individual example EG eye, there were subtle changes for other ONH parameters as well, such as a decrease of the MRA angle (whereby it became significantly more acute at the final session in EG eyes, Fig. 6A), a significant increase in the BMO nonplanarity (whereby the BMO became less planar and more "bowed" into a saddle shape, Fig. 6C) and a significant decrease in the BMO aspect ratio (i.e., the aspect ratio of the best 3D-fit of an ellipse to the BMO, which became rounder, Fig. 6D). However, there was no significant change in the area of the BMO projection (Fig. 6B).

DISCUSSION

The results of this study demonstrated that thinning of the ONH neuroretinal rim is more extensive than thinning of the peripapillary RNFL tissue throughout a wide range of severity in a NHP model of EG. As predicted, the total cross-sectional area of the optical "slice" through these two adjacent tissue sites was similar at baseline in EG and control eyes and remained similar to each other at the final time point in control eyes. In contrast, longitudinal change in EG eyes exhibited substantially greater loss of ONH rim tissue area than peripapillary RNFL tissue area. This finding provided evidence that axon bundles are compressed transversely within the ONH rim as a specific manifestation of glaucomatous deformation. If the only structural change contributing to thinning at each site were loss of retinal ganglion cell axons alone, then their cross-sectional areas should have changed by exactly the same amount.

Several assumptions require consideration, perhaps most important among them is whether the tissue constituents at these two adjacent sites are similar at baseline and whether the nonaxonal constituents change at all or in a similar

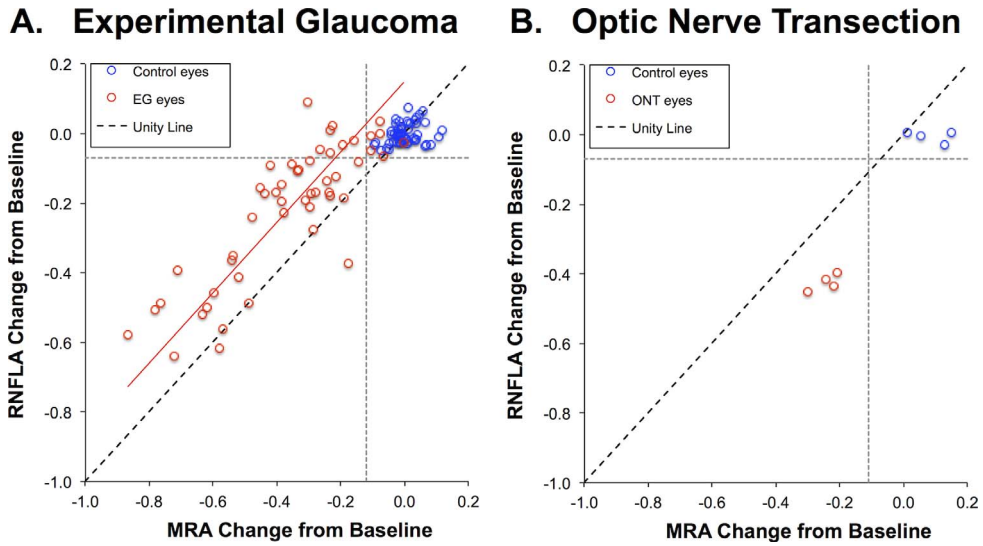

Figure 5. Longitudinal change in MRA is greater than RNFLA in EG, but the opposite pattern occurs after surgical retrobulbar optic nerve transection. (**A**) Scatter plot showing the longitudinal change in RNFLA versus the longitudinal change in MRA for $N = 51$ EG eyes (*red symbols*) and their fellow control eyes (*blue symbols*). The *dashed black diagonal line* represents the 1:1 locus where all points would plot if the MRA change equaled the RNFLA change in each eye. The *solid red line* represents the result of Deming Regression (RNFLA change = 1.01 MRA change + 0.15). Longitudinal change for these two parameters was strongly correlated (Pearson R = 0.84, $P < 0.0001$), but the total cross-sectional area of the ONH rim was 15% less than the total cross-sectional area of the peripapillary RNFL tissue throughout the range of EG severity studied. The *vertical dashed gray line* represents the lower limit of the 95% range of test–retest repeatability for MRA at baseline, while the *horizontal dashed gray line* represents the same for RNFLA. (**B**) Scatter plot showing results of the same analysis for $N = 4$ NHP 50.3 ± 1.0 days after unilateral optic nerve transection; in contrast to EG, this group of eyes shows greater loss of peripapillary RNFLA than loss of ONH MRA ($P = 0.0005$).

manner. First, the ONH rim as measured by the MRA parameter will contain all retinal ganglion cell axons, whereas the peripapillary RNFLA measurement will contain approximately 1.5% fewer axons (since those arising from retinal ganglion cells located between the peripapillary circle scan and the BMO will not contribute). Although it is possible these ganglion cells most proximal to the ONH are at higher risk of degeneration, their number is far too few to account

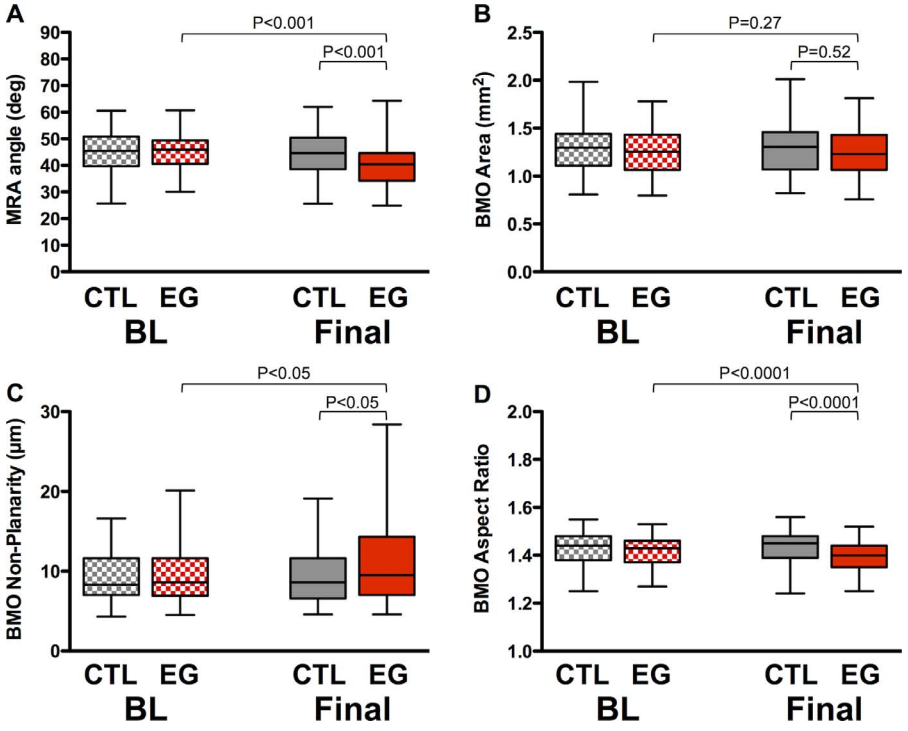

Figure 6. Longitudinal change for other ONH parameters. Box plots represent the distribution (median, interquartile range, and extremes, $N = 51$) of raw parameter values in CTL eyes and eyes with EG at BL (*hatched boxes*) and at the final imaging session (*filled boxes*). (**A**) MRA angle. (**B**) BMO area. (**C**) BMO nonplanarity. (**D**) BMO aspect ratio. The *P* values listed represent the results of a paired *t*-test in each case (comparing EG eyes at the final imaging session to their own BL and separately to their fellow control eyes at the final session; *P* values in red font indicate statistical significance).

for the differential effect observed in this study between MRA and RNFLA.

Second, although the total content of nonaxonal tissue is similar, it is possible that longitudinal changes occur differently at these two sites. The radial peripapillary capillary plexus is the primary circulatory bed serving the RNFL at the site where it was assayed.[29–31] These capillaries are fed by arterioles branching from the central retinal artery, as are the most anterior prelaminar capillaries of the ONH rim tissue with which they are continuous.[15,32] Although ONH capillary volume is thought to decrease following axon loss, capillary density does not change, maintaining a constant ratio of capillary area to neural tissue area.[33,34] This finding is supported further by studies of ONH capillary blood flow.[17,35,36] In fact, there is evidence that ONH capillary blood flow actually increases in the earliest stages of NHP EG,[36] which would be difficult to reconcile if capillary volume within the ONH was reduced dramatically. Nevertheless, ONH capillary loss is unlikely to be so much greater within the ONH rim as compared to the peripapillary RNFL tissue that it could account for the differential observed in this study. For example, recent studies using OCT angiography in glaucoma suggest that loss of capillaries (patent to flow) appears to be continuous between the ONH rim and peripapillary plexuses.[37,38] In fact, the density of ONH vessels patent to flow measured using commercial OCT angiography is effectively a surrogate reflecting ONH rim area,[39] consistent with the earlier demonstration that loss of capillary volume is proportional to loss of neural rim tissue.[33] Indeed, ONH vessel densities measured in glaucomatous eyes by OCT angiography remained within the range of healthy eyes until rim area loss reached a moderate-to-severe stage.[39] Of course, it is possible that ONH tissue compression also might reduce vessel caliber within the rim, but this alone does not seem sufficient to explain the substantial differential documented in this study without also inferring a differential effect on axon caliber within the rim versus the peripapillary RNFL. Moreover, despite being plausible, reduced caliber of capillaries would be inconsistent with the aforementioned evidence from ONH capillary blood flow studies in early-stage NHP EG.[17,35,36]

Third, there is at least one potentially important difference between the ONH rim and peripapillary RNFL in terms of glial content, in that the septa between axon bundles within the RNFL consist of both Muller cell and astrocyte processes whereas the septa separating axon bundles of the ONH rim contain only astrocyte processes.[13,14,40–44] However, overall glial content does not vary significantly between the ONH rim and peripapillary RNFL tissue,[13,14] although it does increase slightly with increased depth into the ONH.[40] In moderate to severe glaucoma, both astrocytes and Muller cells exhibit increased expression of glial fibrillar acidic protein (GFAP) in the retina along with this well-known sign of astrocyte activation within the ONH.[45] However, there is little evidence to suggest that glial content decreases within the ONH rim tissue to a greater extent that it does within the peripapillary RNFL; on the contrary, both sites exhibit hypertrophy of the glial intermediate filament GFAP.[45]

Thus, our findings suggested that axon bundles (and possibly also astrocytes) are compressed (which may represent in part a consequence of longitudinal stretch) within the ONH neuroretinal rim as a result of glaucomatous connective tissue deformation.[46] This may represent a potentially important mechanism of pathophysiologic insult to axons in glaucoma. For decades the primary site of injury in glaucoma was thought to be at the level of the lamina cribrosa.[47–60] Strong evidence supporting this conclusion includes the accumulation of radioactive amino acid tracers and cellular organelles (chiefly swollen, distorted mitochondria but also vesicles) within the posterior aspect of the lamina cribrosa after acute or chronic IOP elevation in NHPs.[48,49,51–57,59] These findings are thought to reflect interruption, or even severe blockade[55] of fast axonal transport at the level of the posterior lamina cribrosa. However, this also is precisely the location where there is normally a very steep gradient of mitochondria between the unmyelinated portion of axons within the prelaminar ONH and the start of myelination in the retrolaminar orbital optic nerve where action potentials abruptly switch to saltatory conduction.[61] Recent evidence from the mouse eye also demonstrates that astrocytes within the myelin transition zone (which extends approximately 1 to 2 mm behind the mouse sclera) are responsible for "recycling" damaged mitochondria from RGC axons by transcellular phagocytosis or "transmitophagy."[62,63]

The phenomenon of transmitophagy in mice suggests that the apparent accumulation of damaged mitochondria (and vesicles laden with membranous debris) within the immediate retrolaminar region of the primate ONH may represent as much a "back-up" of this astrocyte-driven, normal clearance mechanism as it does a primary "back-up" of fast axonal transport. In fact, numerous examples exist within the classic papers on axonal transport interruption in NHP EG models where transport tracers accumulate within the ONH rim tissue (see, e.g., Fig. 2 in the report of Quigley and Anderson[49]; Figs. 3–5 in the report of Quigley and Addicks[57]). The hypothesis that the ONH rim can be a site of injury does not require the rim to be the only site of damage, nor does it undermine the classical evidence from human specimens stained with silver impregnation techniques showing that axons ultimately appear abruptly discontinuous at the posterior aspect of the lamina cribrosa,[50] since this may be the site where injured axons are pruned.[62,63] However, neither do these classic data rule out the possibility that local damage to the axonal cytoskeleton occurs as a direct result of axon deformation (compression and/or stretch) within the ONH rim tissue, with a subsequent predictable failure of axonal transport there as well.

In summary, the results of this study demonstrated that ONH neural rim tissue thinning exceeds peripapillary RNFL thinning over a wide range of severity in NHP EG. These results support the hypothesis that axon bundles (and astrocytes) are compressed (which may include longitudinal stretch) within the ONH rim by glaucomatous connective tissue deformation. This may represent a potentially important mechanism of pathophysiologic insult to axons in glaucoma.

Acknowledgments

The authors thank Galen Williams and Luke Reyes for their expert technical assistance during data collection, as well as Eliesa Ing, MD, and Kevin Ivers, PhD, for their contributions to processing the optic nerve transection data.

Supported by NIH R01-EY019327 (BF), R01-EY011610, and R01-EY021281 (CFB); R01-EY019939 (LW); Legacy Good Samaritan Foundation; Heidelberg Engineering, GmbH, Heidelberg, Germany (equipment and unrestricted research support).

Disclosure: **B. Fortune**, None; **J. Reynaud**, None; **C. Hardin**, None; **L. Wang**, None; **I.A. Sigal**, None; **C.F. Burgoyne**, Heidelberg Engineering, GmbH (F, C, R)

References

1. Sharma P, Sample PA, Zangwill LM, Schuman JS. Diagnostic tools for glaucoma detection and management. *Surv Ophthalmol*. 2008;53(suppl. 1):S17–S32.
2. Leung CK. Diagnosing glaucoma progression with optical coherence tomography. *Curr Opin Ophthalmol*. 2014;25:104–111.

3. Bussel II, Wollstein G, Schuman JS. OCT for glaucoma diagnosis, screening and detection of glaucoma progression. *Br J Ophthalmol*. 2014;98(suppl. 2):ii15–ii19.
4. Fortune B. In vivo imaging methods to assess glaucomatous optic neuropathy. *Exp Eye Res*. 2015;141:139–153.
5. Chauhan BC, Burgoyne CF. From clinical examination of the optic disc to clinical assessment of the optic nerve head: a paradigm change. *Am J Ophthalmol*. 2013;156:218–227, e212.
6. Mwanza JC, Budenz DL. Optical coherence tomography platforms and parameters for glaucoma diagnosis and progression. *Curr Opin Ophthalmol*. 2016;27:102–110.
7. Povazay B, Hofer B, Hermann B, et al. Minimum distance mapping using three-dimensional optical coherence tomography for glaucoma diagnosis. *J Biomed Opt*. 2007;12:041204.
8. Chen TC. Spectral domain optical coherence tomography in glaucoma: qualitative and quantitative analysis of the optic nerve head and retinal nerve fiber layer (an AOS thesis). *Trans Am Ophthalmol Soc*. 2009;107:254–281.
9. Chauhan BC, O'Leary N, Almobarak FA, et al. Enhanced detection of open-angle glaucoma with an anatomically accurate optical coherence tomography-derived neuroretinal rim parameter. *Ophthalmology*. 2013;120:535–543.
10. Gardiner SK, Ren R, Yang H, Fortune B, Burgoyne CF, Demirel S. A method to estimate the amount of neuroretinal rim tissue in glaucoma: comparison with current methods for measuring rim area. *Am J Ophthalmol*. 2014;157:540–549.
11. Danthurebandara VM, Sharpe GP, Hutchison DM, et al. Enhanced structure-function relationship in glaucoma with an anatomically and geometrically accurate neuroretinal rim measurement. *Invest Ophthalmol Vis Sci*. 2015;56:98–105.
12. Fortune B, Hardin C, Reynaud J, et al. Comparing optic nerve head rim width, rim area, and peripapillary retinal nerve fiber layer thickness to axon count in experimental glaucoma. *Invest Ophthalmol Vis Sci*. 2016;57:OCT404–OCT412.
13. Ogden TE. Nerve fiber layer astrocytes of the primate retina: morphology, distribution, and density. *Invest Ophthalmol Vis Sci*. 1978;17:499–510.
14. Ogden TE. Nerve fiber layer of the primate retina: thickness and glial content. *Vision Res*. 1983;23:581–587.
15. Onda E, Cioffi GA, Bacon DR, Van Buskirk EM. Microvasculature of the human optic nerve. *Am J Ophthalmol*. 1995;120:92–102.
16. Patel NB, Luo X, Wheat JL, Harwerth RS. Retinal nerve fiber layer assessment: area versus thickness measurements from elliptical scans centered on the optic nerve. *Invest Ophthalmol Vis Sci*. 2011;52:2477–2489.
17. Cull G, Told R, Burgoyne CF, Thompson S, Fortune B, Wang L. Compromised optic nerve blood flow and autoregulation secondary to neural degeneration. *Invest Ophthalmol Vis Sci*. 2015;56:7286–7292.
18. Told R, Wang L, Cull G, et al. Total retinal blood flow in a nonhuman primate optic nerve transection model using dual-beam bidirectional Doppler FD-OCT and microsphere method. *Invest Ophthalmol Vis Sci*. 2016;57:1432–1440.
19. Ing E, Ivers KM, Yang H, et al. Cupping in the monkey optic nerve transection model consists of prelaminar tissue thinning in the absence of posterior laminar deformation. *Invest Ophthalmol Vis Sci*. 2016;57:2598–2611.
20. Gaasterland D, Kupfer C. Experimental glaucoma in the rhesus monkey. *Invest Ophthalmol*. 1974;13:455–457.
21. Quigley HA, Hohman RM. Laser energy levels for trabecular meshwork damage in the primate eye. *Invest Ophthalmol Vis Sci*. 1983;24:1305–1307.
22. Fortune B, Yang H, Strouthidis NG, et al. The effect of acute intraocular pressure elevation on peripapillary retinal thickness, retinal nerve fiber layer thickness, and retardance. *Invest Ophthalmol Vis Sci*. 2009;50:4719–4726.
23. Strouthidis NG, Fortune B, Yang H, Sigal IA, Burgoyne CF. Effect of acute intraocular pressure elevation on the monkey optic nerve head as detected by spectral domain optical coherence tomography. *Invest Ophthalmol Vis Sci*. 2011;52:9431–9437.
24. Strouthidis NG, Fortune B, Yang H, Sigal IA, Burgoyne CF. Longitudinal change detected by spectral domain optical coherence tomography in the optic nerve head and peripapillary retina in experimental glaucoma. *Invest Ophthalmol Vis Sci*. 2011;52:1206–1219.
25. He L, Yang H, Gardiner SK, et al. Longitudinal detection of optic nerve head changes by spectral domain optical coherence tomography in early experimental glaucoma. *Invest Ophthalmol Vis Sci*. 2014;55:574–586.
26. Fortune B, Burgoyne CF, Cull G, Reynaud J, Wang L. Onset and progression of peripapillary retinal nerve fiber layer (RNFL) retardance changes occur earlier than RNFL thickness changes in experimental glaucoma. *Invest Ophthalmol Vis Sci*. 2013;54:5653–5661.
27. Fortune B, Reynaud J, Wang L, Burgoyne CF. Does optic nerve head surface topography change prior to loss of retinal nerve fiber layer thickness: a test of the site of injury hypothesis in experimental glaucoma. *PLoS One*. 2013;8:e77831.
28. Fortune B, Cull G, Reynaud J, Wang L, Burgoyne CF. Relating retinal ganglion cell function and retinal nerve fiber layer (RNFL) retardance to progressive loss of RNFL thickness and optic nerve axons in experimental glaucoma. *Invest Ophthalmol Vis Sci*. 2015;56:3936–3944.
29. Henkind P. Radial peripapillary capillaries of the retina. I. Anatomy: human and comparative. *Br J Ophthalmol*. 1967;51:115–123.
30. Scoles D, Gray DC, Hunter JJ, et al. In-vivo imaging of retinal nerve fiber layer vasculature: imaging histology comparison. *BMC Ophthalmol*. 2009;9:9.
31. Yu PK, Cringle SJ, Yu DY. Correlation between the radial peripapillary capillaries and the retinal nerve fibre layer in the normal human retina. *Exp Eye Res*. 2014;129:83–92.
32. Wang L, Cull G, Cioffi GA. Depth of penetration of scanning laser Doppler flowmetry in the primate optic nerve. *Arch Ophthalmol*. 2001;119:1810–1814.
33. Quigley HA, Hohman RM, Addicks EM, Green WR. Blood vessels of the glaucomatous optic disc in experimental primate and human eyes. *Invest Ophthalmol Vis Sci*. 1984;25:918–931.
34. Tektas OY, Lutjen-Drecoll E, Scholz M. Qualitative and quantitative morphologic changes in the vasculature and extracellular matrix of the prelaminar optic nerve head in eyes with POAG. *Invest Ophthalmol Vis Sci*. 2010;51:5083–5091.
35. Wang L, Cull GA, Piper C, Burgoyne CF, Fortune B. Anterior and posterior optic nerve head blood flow in nonhuman primate experimental glaucoma model measured by laser speckle imaging technique and microsphere method. *Invest Ophthalmol Vis Sci*. 2012;53:8303–8309.
36. Cull G, Burgoyne CF, Fortune B, Wang L. Longitudinal hemodynamic changes within the optic nerve head in experimental glaucoma. *Invest Ophthalmol Vis Sci*. 2013;54:4271–4277.
37. Jia Y, Wei E, Wang X, et al. Optical coherence tomography angiography of optic disc perfusion in glaucoma. *Ophthalmology*. 2014;121:1322–1332.
38. Liu L, Jia Y, Takusagawa HL, et al. Optical coherence tomography angiography of the peripapillary retina in glaucoma. *JAMA Ophthalmol*. 2015;133:1045–1052.

Investigative Ophthalmology & Visual Science

39. Leveque PM, Zeboulon P, Brasnu E, Baudouin C, Labbe A. Optic disc vascularization in glaucoma: value of spectral-domain optical coherence tomography angiography. *J Ophthalmol*. 2016;2016:6956717.
40. Minckler DS, McLean IW, Tso MO. Distribution of axonal and glial elements in the rhesus optic nerve head studied by electron microscopy. *Am J Ophthalmol*. 1976;82:179–187.
41. Bussow H. The astrocytes in the retina and optic nerve head of mammals: a special glia for the ganglion cell axons. *Cell Tissue Res*. 1980;206:367–378.
42. Ramirez JM, Trivino A, Ramirez AI, Salazar JJ, Garcia-Sanchez J. Immunohistochemical study of human retinal astroglia. *Vision Res*. 1994;34:1935–1946.
43. Trivino A, Ramirez JM, Salazar JJ, Ramirez AI, Garcia-Sanchez J. Immunohistochemical study of human optic nerve head astroglia. *Vision Res*. 1996;36:2015–2028.
44. Balaratnasingam C, Kang MH, Yu P, et al. Comparative quantitative study of astrocytes and capillary distribution in optic nerve laminar regions. *Exp Eye Res*. 2014;121:11–22.
45. Wang L, Cioffi GA, Cull G, Dong J, Fortune B. Immunohistologic evidence for retinal glial cell changes in human glaucoma. *Invest Ophthalmol Vis Sci*. 2002;43:1088–1094.
46. Yang H, Ren R, Lockwood H, et al. The connective tissue components of optic nerve head cupping in monkey experimental glaucoma part 1: global change. *Invest Ophthalmol Vis Sci*. 2015;56:7661–7678.
47. Emery JM, Landis D, Paton D, Boniuk M, Craig JM. The lamina cribrosa in normal and glaucomatous human eyes. *Trans Am Acad Ophthalmol Otolaryngol*. 1974;78:290–297.
48. Anderson DR, Hendrickson A. Effect of intraocular pressure on rapid axoplasmic transport in monkey optic nerve. *Invest Ophthalmol*. 1974;13:771–783.
49. Quigley H, Anderson DR. The dynamics and location of axonal transport blockade by acute intraocular pressure elevation in primate optic nerve. *Invest Ophthalmol*. 1976;15:606–616.
50. Vrabec F. Glaucomatous cupping of the human optic disk: a neuro-histologic study. *Albrecht von Graefes Arch Klin Exp Ophthalmol*. 1976;198:223–234.
51. Minckler DS, Bunt AH, Johanson GW. Orthograde and retrograde axoplasmic transport during acute ocular hypertension in the monkey. *Invest Ophthalmol Vis Sci*. 1977;16:426–441.
52. Quigley HA, Anderson DR. Distribution of axonal transport blockade by acute intraocular pressure elevation in the primate optic nerve head. *Invest Ophthalmol Vis Sci*. 1977;16:640–644.
53. Minckler DS, Bunt AH, Klock IB. Radioautographic and cytochemical ultrastructural studies of axoplasmic transport in the monkey optic nerve head. *Invest Ophthalmol Vis Sci*. 1978;17:33–50.
54. Gaasterland D, Tanishima T, Kuwabara T. Axoplasmic flow during chronic experimental glaucoma. 1. Light and electron microscopic studies of the monkey optic nervehead during development of glaucomatous cupping. *Invest Ophthalmol Vis Sci*. 1978;17:838–846.
55. Quigley HA, Guy J, Anderson DR. Blockade of rapid axonal transport. Effect of intraocular pressure elevation in primate optic nerve. *Arch Ophthalmol*. 1979;97:525–531.
56. Quigley HA, Flower RW, Addicks EM, McLeod DS. The mechanism of optic nerve damage in experimental acute intraocular pressure elevation. *Invest Ophthalmol Vis Sci*. 1980;19:505–517.
57. Quigley HA, Addicks EM. Chronic experimental glaucoma in primates. II. Effect of extended intraocular pressure elevation on optic nerve head and axonal transport. *Invest Ophthalmol Vis Sci*. 1980;19:137–152.
58. Quigley HA, Addicks EM. Regional differences in the structure of the lamina cribrosa and their relation to glaucomatous optic nerve damage. *Arch Ophthalmol*. 1981;99:137–143.
59. Radius RL, Anderson DR. Rapid axonal transport in primate optic nerve. Distribution of pressure-induced interruption. *Arch Ophthalmol*. 1981;99:650–654.
60. Quigley HA, Addicks EM, Green WR, Maumenee AE. Optic nerve damage in human glaucoma. II. The site of injury and susceptibility to damage. *Arch Ophthalmol*. 1981;99:635–649.
61. Barron MJ, Griffiths P, Turnbull DM, Bates D, Nichols P. The distributions of mitochondria and sodium channels reflect the specific energy requirements and conduction properties of the human optic nerve head. *Br J Ophthalmol*. 2004;88:286–290.
62. Nguyen JV, Soto I, Kim KY, et al. Myelination transition zone astrocytes are constitutively phagocytic and have synuclein dependent reactivity in glaucoma. *Proc Natl Acad Sci U S A*. 2011;108:1176–1181.
63. Davis CH, Kim KY, Bushong EA, et al. Transcellular degradation of axonal mitochondria. *Proc Natl Acad Sci. U S A* 2014;111:9633–9638.

Investigative Ophthalmology & Visual Science